MR. XIN AI (Orcid ID : 0000-0003-2227-4574)
PROF. HUI YANG (Orcid ID : 0000-0002-2628-4676)
PROF. YONGMING SUN (Orcid ID : 0000-0001-8528-525X)

Article type : Research Article

Stress-Regulation Design of Lithium Alloy Electrode towards Stable Battery Cycling

Chunhao Li [a], Shuibin Tu [a], Xin Ai [b], Siwei Gui [b], Zihe Chen [a], Wenyu Wang [a], Xiaoxiao Liu [a], Yuchen Tan [a], Hui Yang [b], and Yongming Sun [a]**

C. Li, S. Tu, Z. Chen, W. Wang, Dr. X. Liu, Y. Tan, Prof. Y. Sun
Wuhan National Laboratory for Optoelectronics
Huazhong University of Science and Technology
Wuhan 430074, P. R. China. E-mail: yongmingsun@hust.edu.cn

X. Ai, S. Gui, Prof. H. Yang
State Key Laboratory of Material Processing and Die & Mould Technology, Department of Mechanics, School of Aerospace Engineering
Huazhong University of Science and Technology
Wuhan 430074, P. R. China
E-mail: huiyang2017@hust.edu.cn

Keywords: lithium-ion batteries, lithium alloy, volume expansion/shrinkage, mechanical lithography, stress regulation, chemo-mechanical simulation

Abstract

Metallic tin (Sn) foil is a promising candidate anode for lithium-ion batteries (LIBs) due to its metallurgical processability and high capacity. However, it suffers low initial Coulombic efficiency and inferior cycling stability due to its uneven alloying/dealloying reactions, large volume change and stress, and fast electrode structural degradation. Herein, we report an undulating LiSn electrode fabricated by a scalable two-step procedure involving mechanical lithography and chemical prelithiation of Sn foil. With the combination of experimental measurements and chemo-mechanical simulations, the obtained undulating LiSn/Sn electrode could ensure better mechanical stability due to the pre-swelling state from Sn to Li_xSn and undulating structure of lithography in comparison to plane Sn, homogenize the electrochemical alloying/dealloying reactions due to the activated surface materials, and compensate Li loss during cycling due to the introduction of excess Li from Li_xSn, thus enabling enhanced electrochemical performance. Symmetric cells consisting of undulating LiSn/Sn electrode with an active thickness of ~5 um displayed stable cycling over 1000 hours at 1 mA cm^{-2} and 1 mAh cm^{-2} with a low average overpotential of < 15 mV. When paired with commercial $LiNi_{0.6}Co_{0.2}Mn_{0.2}O_2$ (NCM622) cathode with high mass loading of 15.8 mg cm^{-2}, the full cell demonstrated a high capacity of 2.4 mAh cm^{-2} and outstanding cycling stability with 84.9% capacity retention at 0.5 *C* after 100 cycles. This work presents an advanced LiSn electrode with stress-regulation design toward high-performance LIBs, and sheds light on the rational electrode design and processing of other high-capacity lithium alloy anodes.

1. Introduction

To meet the energy storage demands for ever-increasing application in portable electronics, electric vehicles, and stationary electricity storage, anodes with higher capacity and longer cycle life are desirable to replace graphite in current lithium-ion batteries (LIBs).[1-7] Among the candidates, tin (Sn) stands as a promising material due to its high theoretical capacity of 994 mAh g^{-1} based on the lithiated state of $Li_{4.4}Sn$ and 7246 mAh cm^{-3} based on Sn, which is 2.67 times in mass capacity and almost 10 times in volumetric capacity of graphite.[8-12] Moreover, Sn exhibits an average lithiation potential of ~0.4 V (vs. Li/Li$^+$), which is 0.3 V higher than commercial graphite, and thus could endure large overpotential during battery fast charging or working in low temperature and reduce safety concerns associated with the formation of Li dendrites.[13-15]

However, Sn anode suffers several problems that inherently relates to its high capacity, which heavily hinders its practical application. Huge volume change during charge/discharge processes would cause the fracture and pulverization of Sn anode, leading to poor cycling behaviors.[16] The drastic volume fluctuation of the electrode would also cause the break of solid electrolyte interphase (SEI) on the electrode surface, resulting in continuous side reactions with electrolyte and active lithium (Li) loss featured by low coulombic efficiency on cycling (usually < 99.5%).[17-18] Previous studies had already shown that the structural and interfacial instability could be relieved by the construction of various space-saving nanostructures[19-22] and nanocomposite designs.[23-25] However, high surface area of nanomaterials and severe side reactions with electrolyte always led to low initial Coulombic efficiency, which considerably reduced the reversible capacity of full batteries.[26] Moreover, low compaction density of nanomaterials and introduction of the inert composition of nanocomposites would decrease the volumetric energy density of batteries.[27-28] Therefore, the practical application of Sn anode in high-energy-density LIBs is highly desirable but still challenging.

As opposed to conventional porous electrode configuration, metallic Sn foil is an attracting alternative in consideration of its low accessible surface area to electrolyte, high volumetric energy density, and metallurgical processability.[29] Although Sn foil has long been considered as a high-capacity anode for LIBs, its practical application still faces significant challenges.[30] During the charge/discharge processes, SEI undergoes continuous break and repair, and rapid electrode structural degradation takes place caused by the repeated loading and unloading of high-level stress due to Li insertion/extraction induced large volume change, leading to low initial Coulombic efficiency, continuous Li loss, and inferior cycling performance (Figure 1a). Recently, a mechanical prelithiation approach was explored to address the issue of low initial Coulombic efficiency and significant progress was achieved.[31-33] Further studies should be conducted to address the other issues of fully dense Sn foil to realize its implantation in practical high-energy-density LIBs.

To enhance the structural stability and compensate the active Li loss of Sn foil electrode in full cells, we explored an undulating Li_xSn/Sn electrode with stress-regulation design through scalable roll-to-roll mechanical lithography followed by chemical prelithiation. The undulating structure can effectively regulate the Li insertion/extraction induced stress during the alloying/dealloying reaction, improve the electrolyte wettability, and eliminate the non-uniform lithiation reaction of pristine Sn, which could improve the electrochemical cycling stability and enhance the rate capability of the electrode (Figure 1a). Moreover, the as-formed Li_xSn layer provided additional Li sources to compensate the Li loss during cycling. As expected, the as-achieved undulating LiSn/Sn electrode displayed excellent electrochemical performance. The undulating LiSn/Sn symmetrical cell showed stable cycling at 1 mA cm^{-2} and 1 mAh cm^{-2} for over 1000 hours with a low overpotential below 15 mV. Moreover, a full cell paired with $LiNi_{0.6}Co_{0.2}Mn_{0.2}O_2$ (NCM622) cathode with high mass loading of 15.8 mg cm^{-2} delivered a high initial capacity of 2.4 mAh cm^{-2} and outstanding cycling stability with 84.9% capacity retention at 0.5 *C* after 100 cycles, indicating the promising application in practical high-energy-density LIBs.

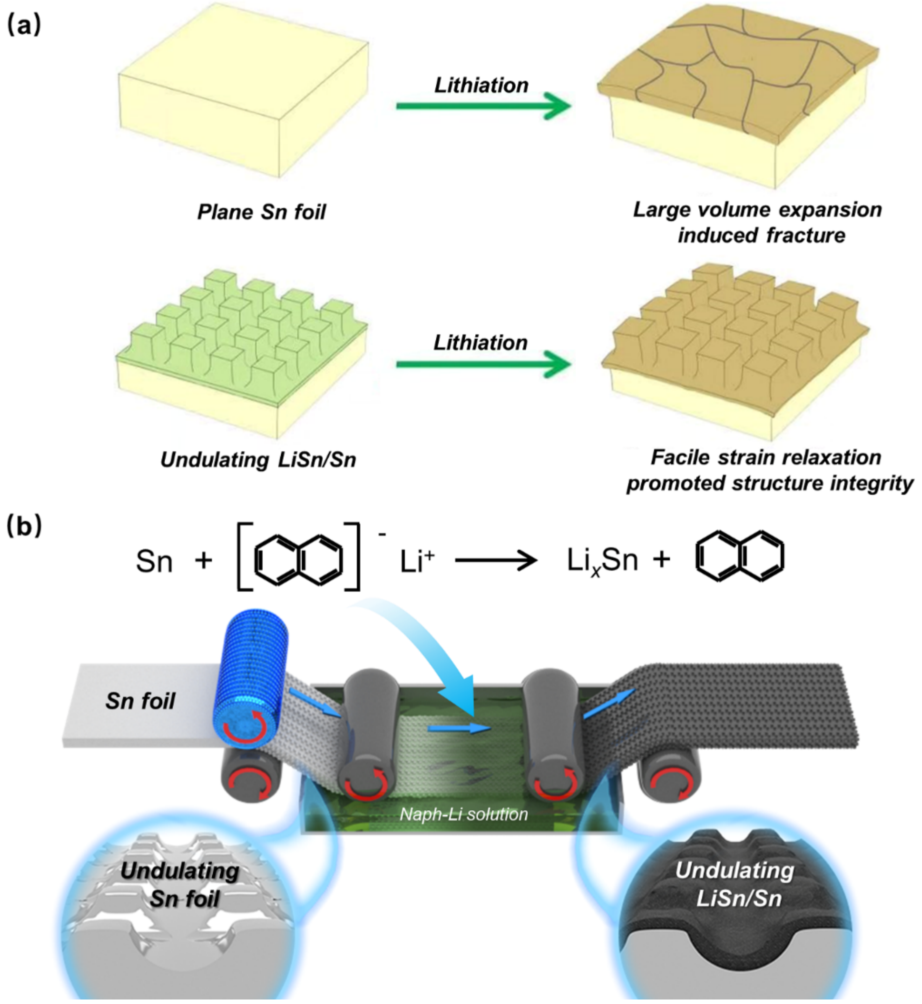

Figure 1. Schematic illustration of a) lithiation behavior of plane Sn foil and undulating Li_xSn/Sn foil, and b) the fabrication of undulating Li_xSn/Sn foil. Undulating Sn foil electrode was fabricated using a roll-to-roll mechanical lithography approach, which was converted to conformal Li_xSn electrode after chemical prelithiation process using Naph-Li solution.

2. Results and Discussion

The undulating Li_xSn/Sn electrode with the stress-regulation design was fabricated by a scalable two-step procedure, including mechanical lithography and subsequent chemical prelithiation (as schematically illustrated in Figure 1b). To generate a desired undulating structure, a roller was first covered by a mesh consisting of micrometer-sized stainless-steel wires. Due to the soft nature of Sn metal, the originally smooth surface of plane Sn foil was inverted into a three-dimensional (3D) continuously undulating Sn structure after mechanical rolling. Naph-Li solution can be stored in ambient air by forming a protective film on the liquid surface, which makes it a potentially practicable prelithiation reagent that can be used in scalable manufactural process.[33] In addition, Sn has various lithiation phases with lithiation potential range between 0.2 and 0.7 V (*vs*. Li/Li^+). A suitable redox potential of ~0.35 V (*vs*. Li/Li^+) for Naph-Li enables moderate lithiation state of Li-Sn alloy (Li_xSn),[34] which can reduce the overall volume change during the subsequent charge (expansion) and discharge (shrinkage) processes in comparison to pure Sn and $Li_{4.4}Sn$ (the full lithiation state). Therefore, Naph-Li solution was chosen for the in-situ conversion of the undulating Sn into undulating Li_xSn/Sn counterpart (Figure 1b).

As shown in Figure 2a, undulating Sn structure was realized after mechanical lithography. The undulating Sn structure remained intact due to the good mechanical processibility of Sn, and its dimension was ~25 μm (Figure 2b and Figure S1). Naph-Li solutions with different concentrations were adopted to produce undulating Li_xSn/Sn electrodes with different reaction times. As seen from Table S1, with the increase of reaction times and concentration of Naph-Li solutions, the preloaded lithium amount for the undulating Li_xSn/Sn electrode increased gradually. The preloaded active lithium-ion capacity using reaction time of 60 min was 1.1 mAh cm^{-2}, which was lower than 2.2 mAh cm^{-2} for that using 35 min. A too long reaction time would lead to the damage of the undulating Li_xSn/Sn electrode, and thus lower the preloaded active lithium-ion capacity. Hence, the undulating Li_xSn/Sn electrodes in the following text were obtained at a prelithiation time of 35 min using 1 M Naph-Li solution. Conformal Li_xSn alloy to the initial Sn foil was generated after chemical prelithiation, featuring a Li_xSn active layer on the Sn substrate. As a whole, the undulating surface structure was well maintained in the as-achieved Li_xSn/Sn foil (Figure 2c, e) and the bottom Sn layer could work as the current collector during the electrochemical charge/discharge cycling. Cross-sectional SEM image of the undulating Li_xSn layer shows intact structure and good uniformity with its thickness of ~5 μm (Figure 2f). For comparison, plane Li_xSn/Sn electrode was also fabricated using plane Sn foil through the same procedure. In contrast, the plane Sn after chemical prelithiation (plane Li_xSn/Sn) showed large cracks on the surface (Figure 2d). Such results indicated the advantage of the undulating surface structure in buffering volume change and ensuring the structure integrity during the expansion of Sn to Li$_x$Sn alloy.

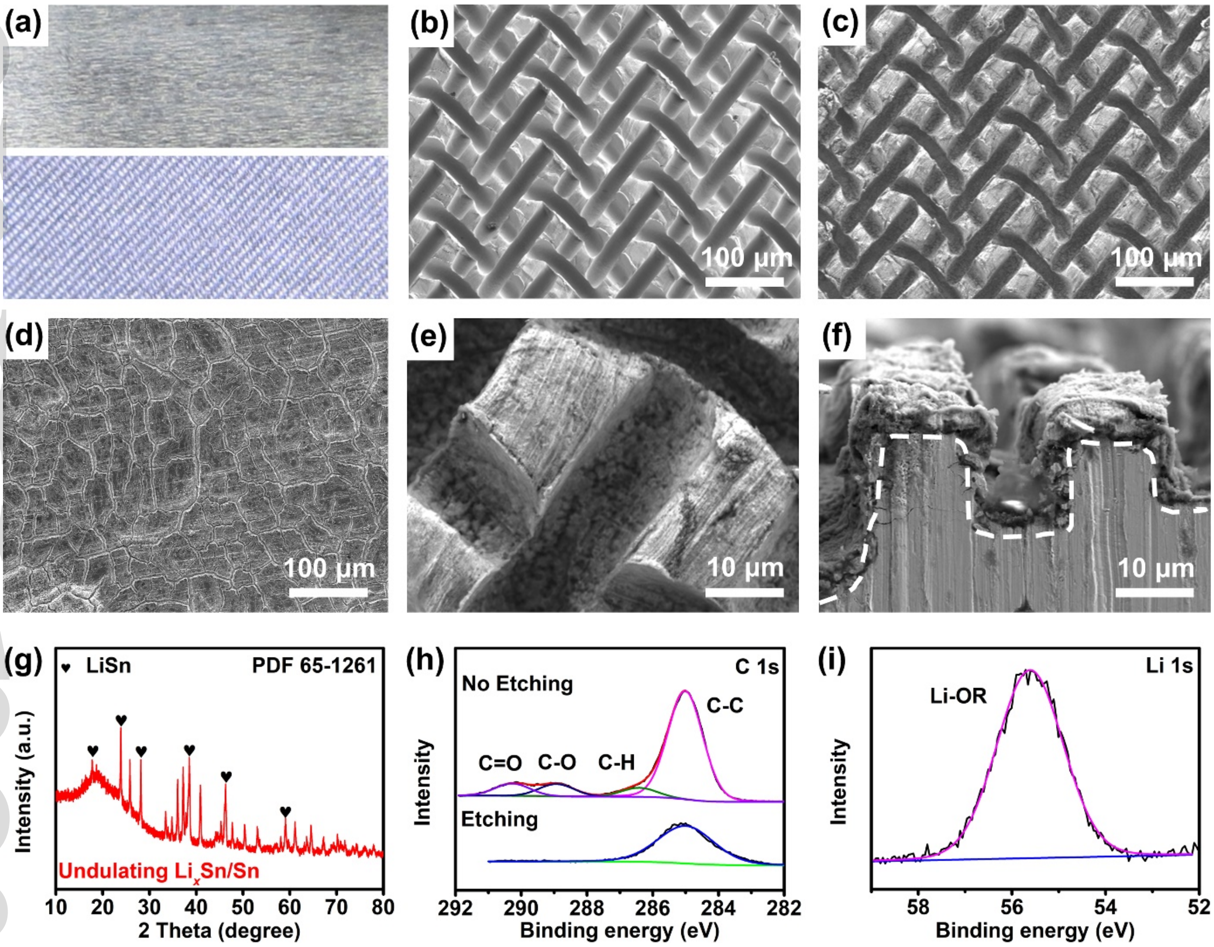

Figure 2. Structure and composition of the as-prepared undulating Li$_x$Sn/Sn electrode. a) Photographs of the plane Sn and undulating Sn foils. b,c,d) SEM images of the undulating Sn (b), undulating Li$_x$Sn/Sn (c), and plane Li$_x$Sn/Sn foils (d) at low magnification. e,f) Top-view (e) and cross-section (f) SEM images of the undulating Li$_x$Sn/Sn foil at high magnification. g) XRD pattern of the undulating Li$_x$Sn/Sn. h) High-resolution C 1s XPS spectra of the undulating LiSn/Sn before and after Ar$^+$ ion-etching. i) High-resolution Li 1s XPS spectrum of the undulating LiSn/Sn.

The composition and crystallinity of the undulating Li$_x$Sn/Sn were further characterized. As shown in Figure 2g, the X-ray diffraction (XRD) peaks of the as-formed prelithiated Sn foil were in good accordance with those of the standard LiSn phase with Sn/Li atomic ratio of 1/1 (PDF65-1261), indicating the successful formation of LiSn after chemical prelithiation. The result of survey X-ray photoelectron spectroscopy (XPS) measurement suggested the co-existence of elemental Sn and Li, again verifying the successful prelithiation of the undulating Sn (Figures S2). Peaks corresponding to Li-OR, C=O and C-O bonding emerged in the XPS spectra (Figure 2h, i and Figure S3), revealing that Li-containing organic compositions, oxides and carbonates might exist on the electrode surface (the as-preformed SEI). The C-H signal in the high-resolution C 1s XPS spectrum may come from the residual naphthalene during the electrode fabrication (Figure 2h). The C=O, C-O and C-H signals disappeared after Ar^+ ion-etching in the high-resolution C 1s XPS spectrum, indicating the organic compositions and carbonates only existed in the surface layer of the electrode. The chemical prelithiation-derived protective layer would cover the surface of the prelithiated anodes, enabling their good stability in dry air condition.[35] In addition, the high-resolution transmission electron microscopy (HRTEM) image in Figure S4 further verified the crystalline nature of the LiSn. The typical interlayer distance of the lithiated product was ~3.75 Å, which agreed well with the separation distance of the (002) lattice plane of crystalline LiSn.

To experimentally verify the synergetic effect of the undulating structure and chemical prelithiation on electrochemical performance, undulating LiSn/Sn||Li half cell and undulating LiSn/Sn symmetric cell were assembled. The amount of stored Li in the undulating LiSn was measured by electrochemical Li extraction measurement at 0.25 mA cm^{-2} by charging a LiSn||Li cell to 2 V (*vs*. Li/Li^+). As shown in Figure 3a, the undulating LiSn exhibited a high Li extraction capacity of ~2.25 mAh cm^{-2}. In contrast, the plane LiSn displayed a much smaller amount of stored active Li (~0.75 mAh cm^{-2}). Undulating LiSn/Sn||Li half cells were then cycled at 0.25 mA cm^{-2} by the first lithiation to an areal capacity of 1 mAh cm^{-2} and then delithiation with a cut-off potential of 2 V (*vs*. Li/Li^+), and the Coulombic efficiency on cycling was recorded. The initial Coulombic efficiency for the undulating LiSn was 95%, much higher than 25% for the pristine undulating Sn foil and 14% for the plane Sn foil (Figure 3b). The much-increased initial Coulombic efficiency should be attributed to the preformed SEI during the chemical prelithiation. Moreover, the activated structure of the undulating LiSn/Sn facilitated the uniform alloy reaction over the entire electrode and suppressed the nonuniform volume change, which further reduced the loss of active Li during cycling. Figure 3c showed the voltage profiles of the undulating LiSn/Sn symmetric cells at 1 mA cm^{-2} with areal capacity fixed at 1 mAh cm^{-2}. The voltage profiles of the 1st, 100th, 250th, and 450th cycle were enlarged in the inset of Figure 3c. The undulating LiSn electrode showed a flat voltage plateau during the charging and discharging processes. The overpotential of the undulating LiSn/Sn during the first cycle was as low as ~25 mV and it decreased to <15 mV and remained stable for more than 1000 hours, indicating a stable electrolyte/electrode interface. The small polarization and stable cycling were further supported by the result of electrochemical impedance spectroscopy (EIS). As shown in Figure 3d, the undulating LiSn/Sn electrode displayed an extraordinary lower impedance of ~30 Ω before cycling. In contrast, the plane Sn foil showed a much larger interfacial resistance of ~120 Ω. Such results suggested better electrode stability and favourable Li lithiation/delithiation kinetics of the undulating LiSn/Sn.

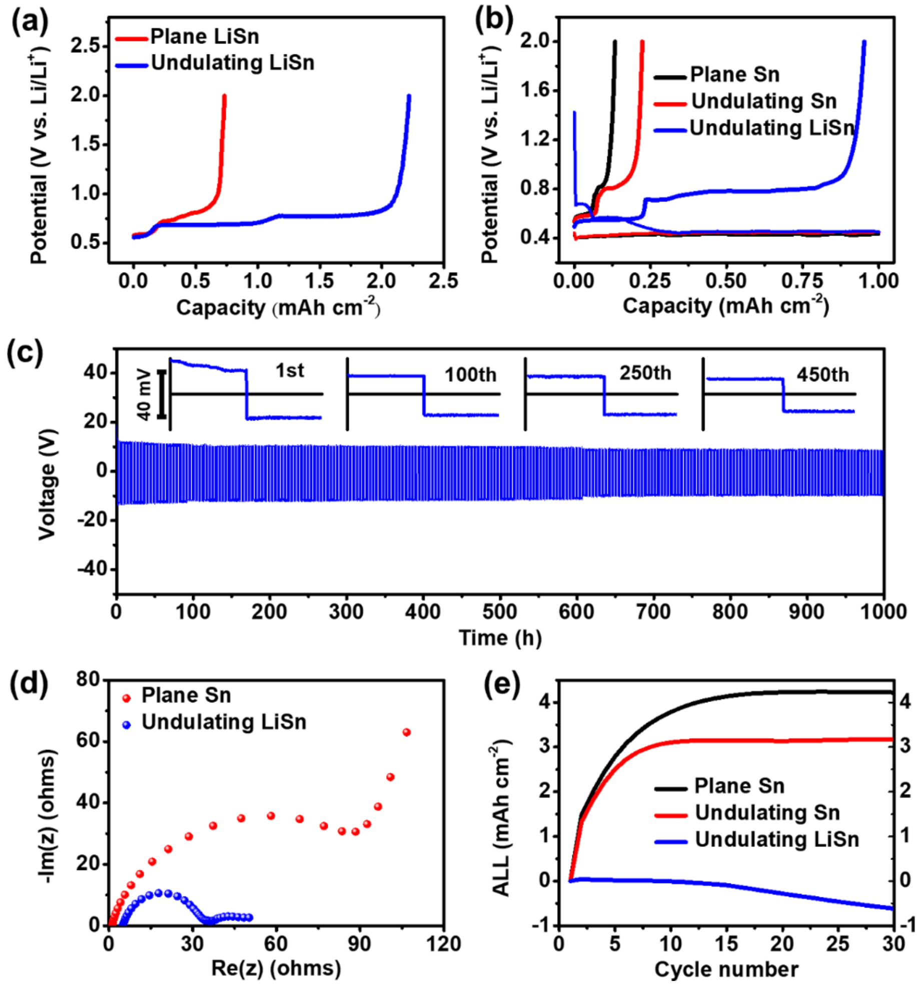

Figure 3. a) Voltage-capacity plot of electrochemical Li extraction process for the undulating LiSn/Sn and plane LiSn/Sn electrodes. b) The first-cycle lithiation/delithiation curves of the plane Sn, undulating Sn, and undulating LiSn/Sn electrodes. c) Voltage-time plots of the undulating LiSn/Sn symmetric cells cycled at 1 mA cm^{-2} and 1 mAh cm^{-2}. d) EIS spectra of the plane Sn and undulating LiSn/Sn electrodes in half cells before cycling. e) The accumulated Li loss of the plane Sn, undulating Sn, and undulating LiSn/Sn electrodes for 30 cycles at 0.25 mA cm^{-2} and 1 mAh cm^{-2}.

Accumulated Li loss on cycling can be an effective indicator to show the stability of the undulating LiSn during electrochemical cycling.[36] With a fixed lithiation capacity of 1 mAh cm^{-2} and cut-off delithiation potential of ~2 V (*vs*. Li/Li^+), the Li-ion capacity difference between lithiation and delithiation for each cycle was recorded as Li loss for the undulating LiSn/Sn, undulating Sn, and plane Sn electrodes in half cell configuration. Figure 3e showed the corresponding accumulated Li loss-cycle number plots for the first 30 cycles. The plane Sn and undulating Sn electrodes exhibited large Li loss in the initial cycles, and the accumulated Li loss for both electrodes increased quickly to ~3.5 mAh cm^{-2} and ~3.0 mAh cm^{-2} in the first 10 cycles, respectively. This trend of increase in accumulated Li loss became slow thereafter and kept almost constant after 15 cycles with values of ~4.0 mAh cm^{-2} and ~3.2 mAh cm^{-2} for the plane Sn and undulating Sn electrodes, correspondingly. The relatively smaller accumulated Li loss for the undulating Sn electrode showed its structural advantage in suppressing side reactions and buffering overall volume change due to the effective strain relaxiation of undulating structure in comparison to the plane Sn electrode. Surprisingly, the accumulated Li loss for the undulating LiSn electrode stayed around 0 in the first 15 cycles, suggesting stable electrochemical lithiation/delithiation behaviors of the LiSn electrode. The accumulated Li loss for the undulating LiSn electrode turned slightly negative in the following cycles, which could be ascribed to the Li compensation effect due to the prestorage of active Li in LiSn/Sn. The high Coulombic efficiency of the undulating LiSn foil during cycling indicated the synergetic contribution of the undulating structure and chemical prelithiation.

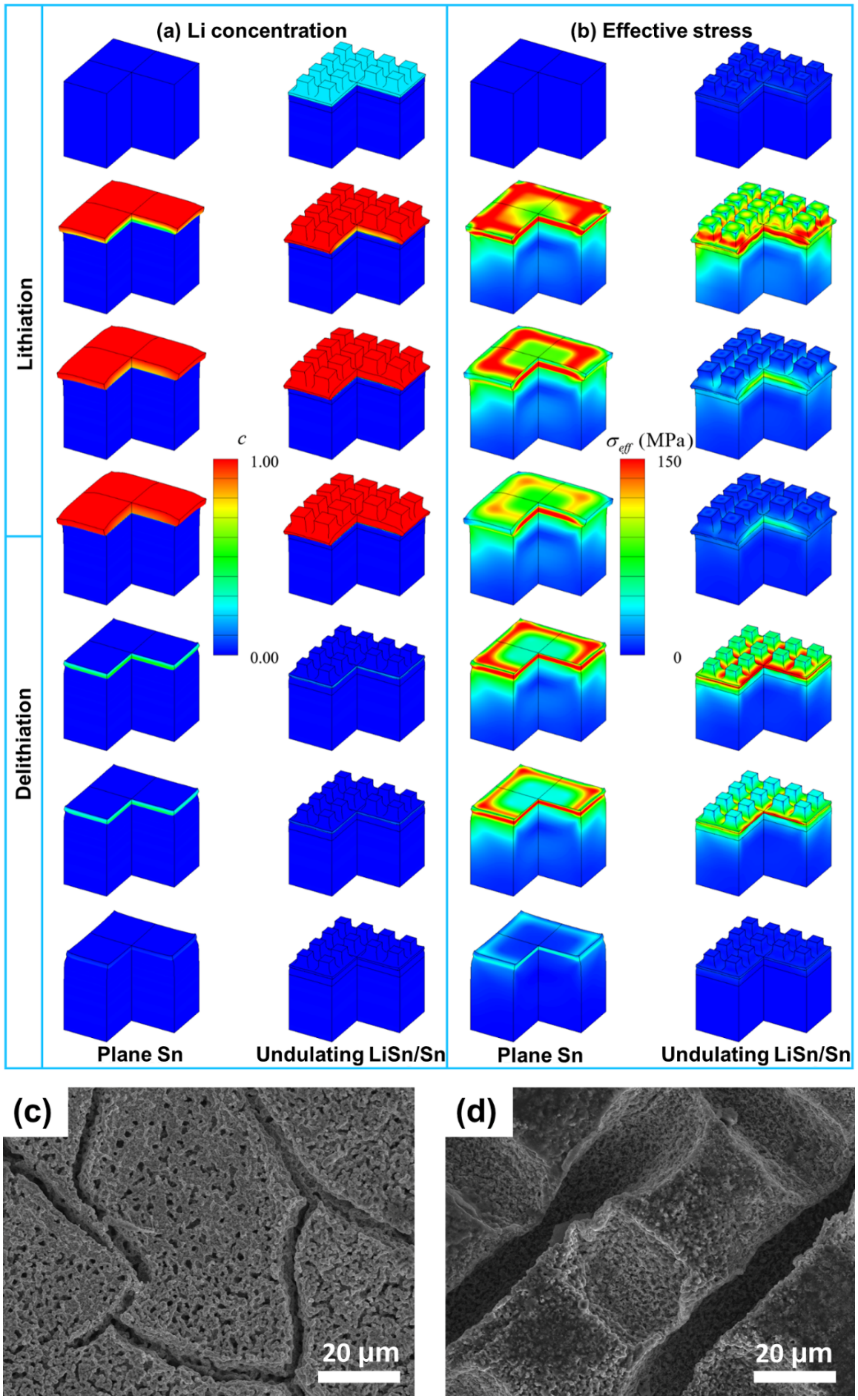

Figure 4. Chemo-mechanical simulated time series snapshots of Li concentration (a) and effective stress (b) distributions in the plane Sn and undulating LiSn/Sn electrodes during lithiation/delithiation cycling. SEM images of the plane Sn (c) and undulating LiSn/Sn electrodes (d) after 30 cycles in half cells.

To uncover the contribution of the undulating LiSn/Sn configuration toward releasing stress and maintaining the integrity of the electrode during electrochemical cycling, chemo-mechanical simulations were conducted by coupling lithiation/delithiation kinetics with elasto-plastic large deformation. Figures 4a and 4b showed the simulated time series snapshots of Li (a) and effective stress (b) distributions in the plane Sn and undulating LiSn/Sn foils. In the Li concentration profiles (Figure 4a), the blue color indicated the unlithiated phase ($c=0$), while the red represented the lithiated phase (assuming $c=1$). The transition colors between red and blue corresponded to the intermediate phases. The corresponding movie (Movie S1) was provided in Supporting Information. During lithiation, Li covered the top surface first and then flowed into the Sn foil, forming a two-phase structure separated by a reaction front. This process was reversed during delithiation, namely, Li was extracted out of the foil from the top surface. For the undulating LiSn foil, the surface-active layer of the foil was firstly lithiated to LiSn ($c=1.0/4.4$) according to the chemical prelithiation process, generating relatively low stress in the foil as shown in Figure 4b. All the foils considered in our simulation were then lithiated to the same final lithiated state (assuming $c=1$). During the following delithiation process, Li concentration in the surface-active layer decreased from $c=1$ to $c=0$. With Li insertion/extraction, high-level effective stress was generated inside the whole surface-active layer of the plane Sn foil, while it only appeared in the bottom region of each column in the undulating LiSn foil. Moreover, for the same lithiation/delithiation capacity, the stress in the undulating LiSn foil could get relaxed much faster than that in the plane Sn foil. Such stress distribution and evolution differences indicated that the surface-active layer of the plane Sn foil always underwent much higher stress than that of the undulating LiSn foil, leading to the widely distributed cracks observed in the postmortem electrode after 30 cycles (Figure 4c and Figure S5). In contrast, the moderate stress in the undulating LiSn foil could well explain the reason why only negligible tiny cracks appeared at the bottom region of the grooves (Figure 4d). In addition, the undulating Sn electrode shows an intact surface compared with that of plane LiSn/Sn electrodes after 30 cycles (Figure S6), further indicating that undulating structure can help to release the stress during the lithiation/delithiation processes. Therefore, the undulating structure in the Sn foil played a significant role in the stress distribution and relaxation during lithiation/delithiation cycling, leading to the robust behavior of the undulating LiSn foil.

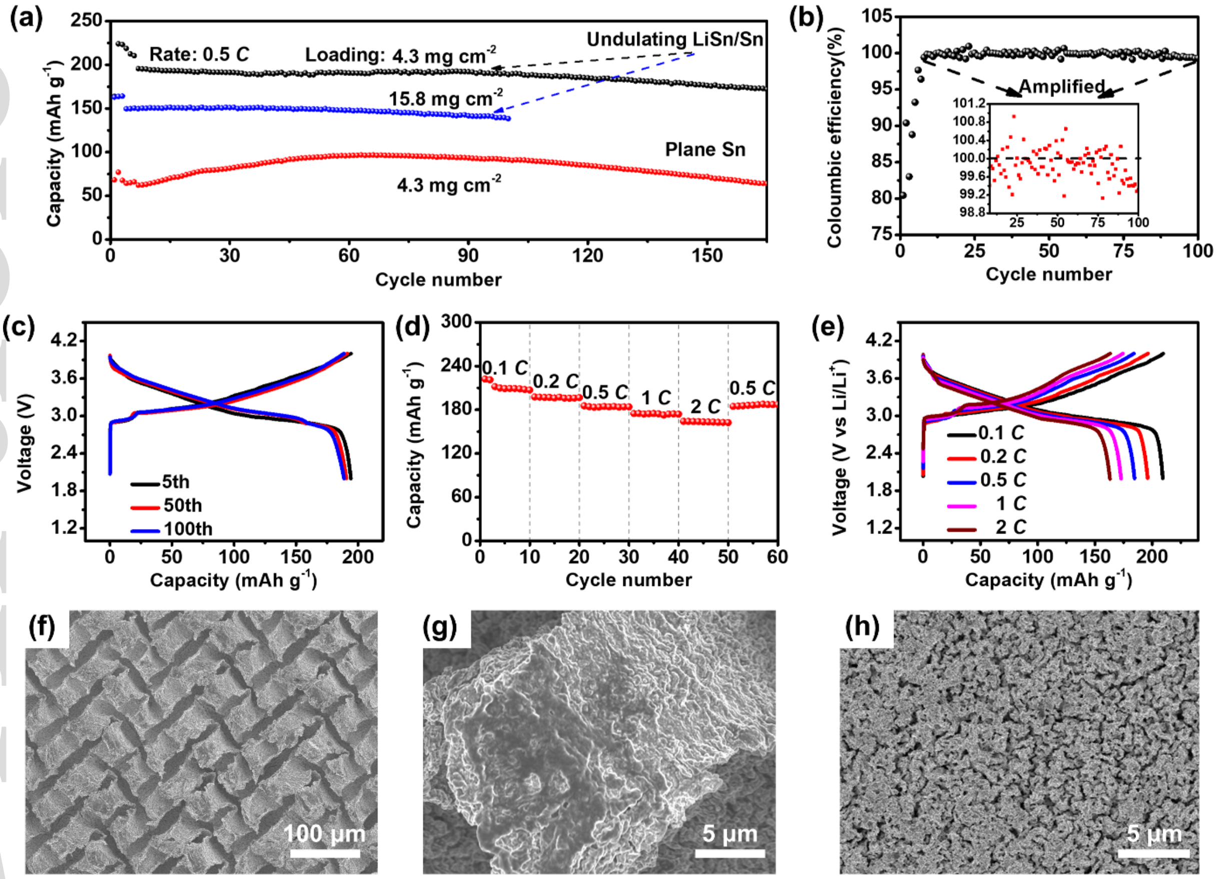

Figure 5. a) Discharge capacity evolutions of the NCM622||undulating LiSn/Sn and NCM622||plane Sn cells at 0.5 *C* for over 100 cycles. b, c) Coulombic efficiency (b) and potential profiles (c) of the NCM622||undualting LiSn/Sn cell. d, e) Discharge capacities of the NCM622||undulating LiSn/Sn cell at different *C* rates (d) and the corresponding charge-discharge curves (e). f, g) SEM images of the undulating LiSn/Sn electrode after 50 cycles at low (f) and high (g) magnification. h) SEM image of the plane Sn electrode after 100 cycles.

To further evaluate the practical application of the undulating LiSn/Sn electrode as a high-performance anode, full cells with the undulating LiSn/Sn electrode as anode and NCM622(mass loading of ~4.3 and 15.8 mg cm^{-2}, respectivly) as cathode were assembled. For comparison, NCM622||plane Sn cells were also fabricated. After 5 activation cycles at 0.1 *C*, the cells were charged/discharged at 0.5 *C* for long-term cycling. Figure 5a showed the capacity-cycle number plots of the NCM622||undulating LiSn and NCM622||plane Sn cells. The NCM622||undulating LiSn cell displayed a reversible capacity of 199.6 mAh g^{-1} with 90% capacity retention after 150 cycles. Even the mass loading of NCM622 cathode increased to 15.8 mg cm^{-2}, it still exhibited a high initial areal capacity of ~2.4 mAh cm^{-2} at 0.5 *C* and high capacity retention of 84.9% after 100 cycles. In contrast, the NCM622||plane LiSn/Sn and NCM622||plane Sn cells with cathode mass loading of ~4.3 mg cm-2 showed inferior electrochemical performance featured with unstable cycling and ultralow specific capacity over the entire measured cycles (Figure 5a and Figure S7). Such a result suggested the advantages of the undulating LiSn/Sn electrode in improving the electrochemical performance of full cells. As shown in Figure 5b, the Coulombic efficiency of the NCM622||undulating LiSn/Sn cell quickly rose above 99.0% in the first 8 cycles, and then maintained at high values between 99.2% and 100.8% in the following cycles, which further revealed the good electrochemical stability of the undulating LiSn structure for high-performance LIBs. Besides, voltage-capacity profiles of the NCM622||undulating LiSn/Sn cell overlapped well on cycling (Figure 5c), further revealing its good electrochemical cycling stability. In contrast, the NCM622||plane Sn cell displayed low Coulombic efficiency below 98% throughout almost the whole tested cycling, and the Coulombic efficiency during the initial 5 cycles was even as low as 47% (Figure S8).

Moreover, the rate capability of the NCM622||undulating LiSn cell was also investigated. Figure 5d and 5e showed the discharge capacity-cycle plots at various *C* rates and the corresponding capacity-voltage plots between 4.0 and 2.0 V. The discharge capacity of the cell gradually decreased from 222 mAh g^{-1} at 0.1 *C* to 197 mAh g^{-1} at 0.2 *C*, 185 mAh g^{-1} at 0.5 *C*, 174 mAh g^{-1} at 1 *C*, and 164 mAh g^{-1} at 2 *C*, respectively. When the rate switched back to 0.5 *C*, the discharge capacity returned to the corresponding original level at 0.5 *C*, indicating admirable reversibility upon cycling. In contrast, the NCM622||plane Sn cell showed inferior rate capability and capacity fluctuation (Figure S9). Such phenomenon might be attributed to the unstablity of the plane Sn anode, in accordance with the unstable electrochemical cycling results shown in Figure 5a.

To verify the good stability of the undulating LiSn electrode, the structure and morphology of the undulating LiSn electrode after 100 cycles were investigated. Figures 5f and 5g showed the SEM images of the undulating LiSn electrode after 100 cycles at 0.5 *C*. The undulating LiSn electrode maintained good structural integrity with overall morphology unchanged after cycling (Figure 5f), although the surface of the undulating structure became slightly rougher (Figure 5g) in comparision to the original undulating LiSn electrode (Figure 2d), supporting the excellent performance of the undulating LiSn electrode. In sharp contrast, extensive cracks and voids in micrometer size showed up in the plane Sn electrode under the same test conditions (Figure 5h), suggesting the unstable plane Sn electrode structure during cycling.

3. Conclusion

In summary, we proposed a strategy of undulating structure design and using LiSn as the active material to realize stable cycling of high-capacity Sn-based battery anode. A scalable two-step procedure including mechanical lithography and subsequent chemical prelithiation of metallic Sn is presented in this study to fabricated undulating LiSn anode. Benefiting from the undulating electrode structure with moderate pre-swelling design, the strain caused by volume change during the charge/discharge cycle was effectively relaxed for the undulating LiSn/Sn electrode, leading to long-term chemo-mechanical stability and structural integrity of the LiSn electrode. Moreover, the chemical prelithiation of Sn provided additional Li to compensate the Li loss during the charge/discharge cycling, enabling the improvement of the initial Coulombic efficiency of Sn foil electrode and cycle lifespan of full cells. NCM622||undulating LiSn/Sn cell with cathode mass loading of 15.8 mg cm^{-2} delivered a high initial capacity of 2.4 mAh cm^{-2} and demonstrated outstanding cycling stability with 84.9% capacity retention at 0.5 *C* after 100 cycles. This work provides an alternative strategy to address the chemo-mechanical failure and improve alloy-based anode by using a stress-regulation geometry structure design in combination with a moderate pre-swelling Li alloy state.

4. Experimental Section

The preparation of undulating LiSn/Sn electrodes:

Stainless steel mesh (500 mesh, Jiangsu Wanhu Materials Co. Ltd) was attached on a roller of a rolling machine. A commercial Sn foil (Fuxiang Materials Co. Ltd) was calendared using the rolling machine with controlled rolling distance, and an undulating Sn structure with an inverse mesh structure was achieved. 1M Li naphthalene (Naph-Li) solution was prepared by adding lithium metal slice in a solution of naphthalene (Naph, Innochem, 99%) in tetrahydrofuran (THF, Sigma-Aldrich, ≥99.9%) in an Ar-filled glove box. The undulating Sn electrode were rested in the as-prepared 1 M Naph-Li solution for a designed duration time to produce undulating Li$_x$Sn/Sn electrode, and then washed with THF for three times in the Ar-filled glove box.

***Materials characterization*:** Scanning electron microscopy (SEM) images were conducted for morphology characterization using a Gemini SEM300 with an energy spectrometer (Nova NanoSEM 450). To investigate the phase information of the products, X-ray diffraction (XRD) measurement was carried out on an X'Pert PRO diffractometer (PANalytical B.V., Holland) with Cu-Kα1 radiation operated at an accelerating voltage of 40 kV and a current of 40 mA. X-ray photoelectron spectroscopy (XPS) analyses were performed on a VG Multilab 2000 system (Thermo VG Scientific) for the composition and surface electron state of the materials. For the characterization of the electrodes after cycling, cells were first disassembled and the electrodes were washed with 1,3-Dioxolane (DOL) and dried in Ar filled glove box.

***Electrochemical characterization*:** The undulating LiSn/Sn, undulating Sn and plane Sn foils were directly used as electrodes for electrochemical measurements. The NCM622 cathode consisted of 10 wt% carbon black as the conductive additive, 10 wt% Polyvinylidene fluoride (PVDF) as the binder, and 80 wt% commercial NCM622 powder as the active material. It was prepared using a slurry casting method using N-Methyl-2-pyrrolidone (NMP) as a solvent for the slurry fabrication. The slurry was coated on an aluminum foil and the electrode was dried at 60 ºC under vacuum for 4 h. The typical mass loading of NCM622 in cathode was ~4.3 mg cm^{-2} and ~15.8 mg cm^{-2}, respectively. The specific capacity and the applied current density were all calculated based on the mass of NCM622 in the cathode. Coin cells of CR2032 were assembled in an argon-filled glove box (H_2O and O_2 < 0.1 ppm). The electrolyte was 1 M Li hexafluorophosphate ($LiPF_6$) in 1:1:1 ethylene carbonate (EC)/propylene carbonate (PC)/diethyl carbonate (DEC) with 10% fluoroethylene carbonate (FEC) and 1% vinylene carbonate (VC). Celgard 2300 (19 μm, PP/PE/PP) was adopted as the separator. Galvanostatic charge-discharge measurement was conducted on Neware battery tester (Neware, China) at room temperature for electrochemical evaluation. Electrochemical impedance spectrometry (EIS) test was carried out on a Biologic VMP3 system with a frequency range of 100 kHz to 100 mHz. The undulating LiSn/Sn symmetric cells were cycled with a current density of 1 mA cm^{-2} and 1 mAh cm^{-2}. The full cells were cycled in the voltage range of 2.0–4.0 V *vs*. Li$^+$/Li at various *C* rates.

***Chemo-mechanical simulation*:** A recently developed continuum chemo-mechanical model was implemented in ABAQUS to simulate the concurrent processes of phase transformation, stress generation, and morphological evolution of the Sn foils during lithiation/delithiation cycling.[33-34] In this model, the lithiation/delithiation process is governed by:

$$\begin{cases} \dfrac{\partial c}{\partial t} = -\nabla \cdot \mathbf{J} \\ \nabla \cdot \boldsymbol{\sigma} = 0 \end{cases} \qquad (1)$$

where, c is the local normalized Li concentration defined as the actual Li concentration divided by the maximum Li concentration at the fully lithiated stage, which varies from 0 (representing the unlithiated phase) to 1 (representing the fully lithiated phase), $\mathbf{J} = D \cdot \nabla c$ is the Li flux, with the stress-free Li diffusivity, D, set to be a nonlinear function of Li concentration: [37-39]

$$D = D_0\left[\frac{1}{(1-c)} - 2\alpha c\right] \qquad (2)$$

where, D_0 is a diffusion constant and α is a tunable constant that controls the concentration profile near the phase boundary. $\boldsymbol{\sigma}$ is the Cauchy stress tensor and ∇ represents the vector differential operator with respect to spatial coordinates. The total strain tensor $\boldsymbol{\varepsilon}$ is given by: $\boldsymbol{\varepsilon} = \boldsymbol{\varepsilon}^{el} + \boldsymbol{\varepsilon}^{pl} + \boldsymbol{\varepsilon}^{cr} + \boldsymbol{\varepsilon}^{ch}$, in which $\boldsymbol{\varepsilon}^{el}$ is the elastic strain, $\boldsymbol{\varepsilon}^{pl}$ is the plastic strain, $\boldsymbol{\varepsilon}^{cr}$ is the creep strain, and $\boldsymbol{\varepsilon}^{ch} = \beta c\mathbf{I}$ is the chemical strain. Here β is the expansion coefficient and $\mathbf{I}$ is the identity tensor. As Li insertion/extraction can induce elasto-plastic large deformation in Sn, the finite-strain plasticity theory with the J_2 flow rule is employed. The creep strain rate is defined by: $\dot{\boldsymbol{\varepsilon}}^{cr} = \frac{3}{2}\frac{\boldsymbol{\sigma}'}{\sigma_e}\dot{\bar{\varepsilon}}^{cr}$, where $\boldsymbol{\sigma}'$ is the deviatoric stress tensor, σ_e is the von Mises equivalent stress, and $\dot{\bar{\varepsilon}}^{cr} = A\sigma_e^n$ is the equivalent creep strain rate with A and n two material parameters.[40] With pertinent boundary and initial conditions, the chemo-mechanical coupling problem was solved by the temperature-displacement procedure in ABAQUS/Standard with user subroutines used to interface with ABAQUS to dynamically update the diffusivity and flux based on the instantaneous Li profile.

A 3D model with a 5 μm prelithiated surface layer was constructed to simulate the lithiation/delithiation behaviors of the undulating LiSn/Sn electrode. For comparison, the plane Sn foil (without prelithiation) was also considered, with the surface active layer set to be 8.24 μm to ensure the same electrochemical loading as that of the undulating LiSn electrode. In each model, the bottom surface of the foil was fixed and the lateral surface was set to be free. On the top surface that Li was inserted into (or extracted out of) the Sn foil during lithiation (or delithiation) process, the Dirichlet boundary condition for Li concentration was applied. All the material parameters were specified according to experimental data whenever possible.[41-42] Specifically, the Young's modulus and Poisson's ratio of the lithiated product of Sn were both assumed to linearly vary with Li concentration, i.e., from 50 to 28 GPa and from 0.33 to 0.15, respectively, as the normalized Li concentration c varied from 0 (c-Sn) to 1 (the fully lithiated phase). The two creep parameters, A and n, were set to be 2.3×10^{-8} and 1.5, respectively, and the yield stress was assumed to be a constant 150 MPa. To ensure the ~260% volume expansion for the fully lithiated Sn phase,[43] the expansion coefficient β was set to be 0.42.

Supporting Information

Supporting Information is available from the Wiley Online Library or from the author.

Acknowledgements

This work is financially supported by the Natural Science Foundation of China (Grant No. 51802105) and China Postdoctoral Science Foundation. The authors would also like to thank the Analytical and Testing Center of Huazhong University of Science and Technology (HUST) as well as the Center for Nanoscale Characterization & Devices of Wuhan National Laboratory for Optoelectronics (WNLO) for providing the facilities to conduct the characterizations.

Conflict of Interest

The authors declare no conflict of interest.

Received: ((will be filled in by the editorial staff))
Revised: ((will be filled in by the editorial staff))
Published online: ((will be filled in by the editorial staff))

References

[1] Y. Sun, N. Liu, Y. Cui, *Nat. Energy* **2016**, 1, 16071.

[2] A. Kwade, W. Haselrieder, R. Leithoff, A. Modlinger, F. Dietrich, K. Droeder, *Nat. Energy* **2018**, 3, 290.

[3] M. Li, J. Lu, Z. Chen, K. Amine, *Adv. Mater.* **2018**, 1800561.

[4] S. Tu, X. Chen, X. Zhao, M. Cheng, P. Xiong, Y. He, Q. Zhang, Y. Xu, *Adv. Mater.* **2018**, 30, 1804581.

[5] M. Winter, B. Barnett, K. Xu, *Chem. Rev.* **2018**, 118, 11433.

[6] T. Chen, Y. Jin, H. Lv, A. Yang, M. Liu, B. Chen, Y. Xie, Q. Chen, *Trans. of Tianjin Univ.* **2020**, 26, 208.

[7] S. Wang, Q. Liu, C. Zhao, F. Lv, X. Qin, H. Du, F. Kang, B. Li, *Energy & Environ. Mater. 2018, 1, 28.*

[8] C. M. Park, J. H. Kim, H. Kim, H. J. Sohn, *Chem. Soc. Rev.* **2010**, 39, 3115.

[9] F. Xin, M. S. Whittingham, *Electrochem. Energy Rev.* **2020**, 3, 643.

[10] W.-J. Zhang, *J. Power Sources* **2011**, 196, 13.

[11] Y. Liu, Z. Tai, T. Zhou, V. Sencadas, J. Zhang, L. Zhang, K. Konstantinov, Z. Guo, H. K. Liu, *Adv. Mater.* **2017**, 29, 1703028.

[12] Y. Wu, X. Huang, L. Huang, J. Chen, *Energy & Environ. Mater. 2021, 4, 19.*

[13] B. Huang, Z. Pan, X. Su, L. An, *J. Power Sources* **2018**, 395, 41.

[14] Z. Yi, Z. Wang, Y. Cheng, L. Wang, *Energy & Environ. Mater.* **2018**, 1, 132.

[15] S. Guo, Y. Feng, L. Wang, Y. Jiang, Y. Yu, X. Hu, *Small* **2021**, 2005248.

[16] H. Ying, W.-Q. Han, *Adv. Sci.* **2017**, 4, 1700298.

[17] N. Zhang, C. Sun, Y. Huang, C. Zhu, Z. Wu, L. Lv, X. Zhou, X. Wang, X. Xiao, X. Fan, L. Chen, *J. Mater. Chem. A* **2021**, 9, 1812.

[18] J. Huang, X. Guo, X. Du, X. Lin, J.-Q. Huang, H. Tan, Y. Zhu, B. Zhang, *Energy & Environ. Sci.* **2019**, 12, 1550.

[19] J. Han, D. Kong, W. Lv, D. M. Tang, D. Han, C. Zhang, D. Liu, Z. Xiao, X. Zhang, J. Xiao, X. He, F. C. Hsia, C. Zhang, Y. Tao, D. Golberg, F. Kang, L. Zhi, Q. H. Yang, *Nat. Commun.* **2018**, 9, 402.

[20] F. Maroni, P. Bruni, N. Suzuki, Y. Aihara, F. Croce, *J. Solid State Electrochem.* **2019**, 23, 1697.

[21] Z. Li, Q. Yin, W. Hu, J. Zhang, J. Guo, J. Chen, T. Sun, C. Du, J. Shu, L. Yu, J. Zhang, *J. Mater. Sci.* **2019**, 54, 9025.

[22] Z. Wang, K. Dong, D. Wang, S. Luo, Y. Liu, Q. Wang, Y. Zhang, A. Hao, C. Shi, N. Zhao, *J. Mater. Chem. A* **2019**, 7, 14309.

[23] T. L. Nguyen, D. S. Kim, J. Hur, M. S. Park, I. T. Kim, *Electrochim. Acta* **2018**, 278, 25.

[24] M. G. Park, D. H. Lee, H. Jung, J. H. Choi, C. M. Park, *ACS Nano* **2018**, 12, 2955.

[25] H. Shi, Z. Fang, X. Zhang, F. Li, Y. Tang, Y. Zhou, P. Wu, G. Yu, *Nano Lett.* **2018**, 18, 3193.

[26] C. Wang, H. Wu, Z. Chen, M. T. McDowell, Y. Cui, Z. Bao, *Nat. Chem.* **2013**, 5, 1042.

[27] H. Liu, X. Cheng, Y. Chong, H. Yuan, J.-Q. Huang, Q. Zhang, *Particuology* **2021**, 57, 56.

[28] S. T. Boles, M. H. Tahmasebi, *Joule* **2020**, 4, 1.

[29] S. Tu, X. Ai, X. Wang, S. Gui, Z. Cai, M. Zhan, Y. Tan, W. Liu, H. Yang, C. Li, Y. Sun, *J. Energy Chem.* **2021**, 62, 477.

[30] H. Xu, S. Li, C. Zhang, X. L. Chen, W. J. Liu, Y. H. Zheng, Y. Xie, Y. H. Huang, J. Li, *Energy & Environ. Sci.* **2019**, 12, 2991.

[31] H. Xu, S. Li, X. Chen, C. Zhang, W. Liu, H. Fan, Y. Yu, Y. Huang, J. Li, *Adv. Energy Mater.* **2019**, 1902150.

[32] H. Xu, S. Li, X. Chen, C. Zhang, Z. Tang, H. Fan, Y. Yu, W. Liu, N. Liang, Y. Huang, J. Li, *Nano Energy* **2020**, 74, 104815.

[33] G. Wang, F. Li, D. Liu, D. Zheng, Y. Luo, D. Qu, T. Ding, D. Qu, ACS Appl. Mater. Interfaces 2019, 11, 8699.

[34] Y. F. Shen, J. M. Zhang, Y. F. Pu, H. Wang, B. Wang, J. F. Qian, Y. L. Cao, F. P. Zhong, X. P. Ai, H. X. Yang, *Acs Energy Letters* **2019**, 4, 1717.

[35] J. Jang, I, Kang, J. Choi, H. Jeong, K-W. Yi, J. Hong, M. Lee, Angew.Chem. Int. Ed. 2020, 59,14473.

[36] Y. Jin, S. Li, A. Kushima, X. Zheng, Y. Sun, J. Xie, J. Sun, W. Xue, G. Zhou, J. Wu, F. Shi, R. Zhang, Z. Zhu, K. So, Y. Cui, J. Li, *Energy & Environ. Sci.* **2017**, 10, 580.

[37] H. Yang, F. Fan, W. Liang, X. Guo, T. Zhu, S. Zhang, *J. Mech. Phys. Solids* **2014**, 70, 349.

[38] X. Shi, J. Zhu, Y. Xia, F. Fan, F. Zhang, M. Gu, H. Yang, *ACS Appl. Energy Mater.* **2018**, 1, 4211.

[39] H. Yang, S. Huang, X. Huang, F. Fan, W. Liang, X. H. Liu, L.-Q. Chen, J. Y. Huang, J. Li, T. Zhu, S. Zhang, *Nano letters* **2012**, 12, 1953.

[40] ABAQUS, *Dassault Systemes Simulia Corp., Providence, RI, USA* **2010**.

[41] R. Hu, M. Zhu, H. Wang, J. Liu, O. Liuzhang, J. Zou, *Acta Mater.* **2012**, 60, 4695.

[42] C. S. Hong, N. Qaiser, H. G. Nam, S. M. Han, *Phys. Chem. Chem. Phys.* **2019**, 21, 9581.

[43] J. Wang, F. Fan, Y. Liu, K. L. Jungjohann, S. W. Lee, S. X. Mao, X. Liu, T. Zhu, *J. Electrochem. Soc.* **2014**, 161, F3019.